# On Atomistic Models for Molecular Oxygen

Matti Javanainen,[†,‡] Ilpo Vattulainen,[†,‡,¶] and Luca Monticelli[*,§]

†*Department of Physics, Tampere University of Technology, Tampere, Finland*

‡*Department of Physics, University of Helsinki, Helsinki, Finland*

¶*MEMPHYS - Centre for Biomembrane Physics, University of Southern Denmark, Odense, Denmark*

§*University of Lyon, CNRS, UMR 5086 MMSB, Lyon, France*

E-mail: luca.monticelli@inserm.fr

**Abstract**

Molecular oxygen ($O_2$) is key to all life on earth as it is constantly cycled via photosynthesis and cellular respiration. Substantial scientific effort has been devoted to understanding every part of this cycle. Classical molecular dynamics (MD) simulations have been used to study some of the key processes involved in cellular respiration: $O_2$ permeation through alveolar monolayers and cellular membranes, its binding to hemoglobin during transport in the bloodstream, as well as as its transport along optimal pathways towards its reduction sites in proteins. Moreover, MD simulations can help interpreting the results of several imaging techniques, where $O_2$ is used due to its paramagnetic nature. However, despite the widespread use of computational models for the $O_2$ molecule, their performance has never been systematically evaluated. In this paper, we assess the performance of 14 different models of $O_2$ available in the literature by calculating four thermodynamic properties: density, heat of vaporization, free energy of hydration, and free energy of solvation in hexadecane. For each property, reliable experimental data are available. Most models perform reasonably well in predicting the correct trends, but they fail to reproduce the experimental data quantitatively. We then develop new models for $O_2$, with and without a quadrupole moment, and compare their behavior with the behavior of previously published models. The new models show significant improvement in terms of density, heat of vaporization, and free energy of hydration. However, quantitative agreement with water–oil partitioning is not reached due to discrepancies between the calculated and measured free energy of solvation in hexadecane. We suggest that classical pairwise-additive models may be inadequate to properly describe the thermodynamics of solvation of apolar species, such as $O_2$, in apolar solvents.

# Introduction

Molecular oxygen (also known as dioxygen, $O_2$) constitutes about 20% of the air we breathe, and it is the key molecule in respiration. The dioxygen molecule has a quadrupole moment

but no permanent dipole, therefore it is largely non-polar. Its non-polar character is also evident from its partitioning behavior: indeed oxygen partitions more favorably into oil than into water, as found experimentally.[1,2] As a consequence, oxygen is highly soluble in lipid membranes and permeates through them very easily[3] – a property with important biological implications. By virtue of its electronic structure, molecular oxygen is also widely used in structural biology: the lowest-energy electronic state (ground state) of molecular oxygen is a triplet state, and it is paramagnetic. Paramagnetism and high solubility of dioxygen in lipid membranes have been used to probe the structure, the orientation, and the interactions of membrane proteins using Electron Spin Resonance (ESR) and Nuclear Magnetic Resonance (NMR) techniques.[4–7] In both cases, measurements of relaxation times in the presence of paramagnetic probes provide information on accessibility of specific residues to the probe, and therefore on fine details of membrane protein structure. Since $O_2$ has a pronounced solubility gradient in membranes, analysis of NMR relaxation rates in the presence of $O_2$ provides information on the depth of individual spin-active nuclei in a membrane, and therefore on protein topology and orientation.[7]

Interpretation of the results from magnetic resonance techniques relies on molecular models and greatly benefits from the use of molecular simulations. Molecular simulations, in turn, require realistic models for all molecules in the system of interest. In the case of simulations including the dioxygen molecule, it is crucial that models reproduce the correct partitioning of the dissolved gas between water and a membrane.

Several molecular models of $O_2$, summarized in Table 1, have been proposed in the literature.[8–17] These models have been employed extensively *e.g.* in studies on membrane permeation related to cellular respiration[8,16,18–24] as well as to study the interactions of oxygen with membrane proteins, notably the pathways of oxygen to reduction or binding sites of numerous proteins[9,14,25–42] (see also recent reviews[43,44]). However, despite the widespread use of such models, their performance – including the crucial partitioning data – has never been systematically evaluated, to the best of our knowledge.

In the present report we examine the performance of a large set of existing models of molecular oxygen in reproducing fundamental thermodynamic properties: density, heat of vaporization, and free energies of solvation in water and hexadecane. Densities and heats of vaporization are generally used as target properties in the parameterization of non-bonded interactions of pure liquids.[45] Free energies of hydration are often used to validate force field parameters,[46–49] but matching the free energy of hydration is not sufficient to guarantee the correct partitioning between water and lipid membranes. On the other hand, precise data for the free energy of transfer from water to membranes is not available from experiments. Therefore we use water–alkane partitioning as a proxy for water–membrane partitioning. This choice is justified by the clear correlation between water–alkane partitioning coefficients and membrane permeabilities.[50] Our results show that none of the models available from the literature reproduce quantitatively all four target properties, and most models show errors larger than 10% in either density or heat of vaporization. We then report on the optimization of two dioxygen models – with and without a quadrupole moment. Both new models show good agreement with experimental density and heat of vaporization. However, neither the models from the literature nor the ones developed here reproduce quantitatively the free energy of transfer between water and alkanes, suggesting that limitations may be inherent in pairwise additive models.

# Thermodynamics of solvation and transfer

Abraham *et al.* reported the partition coefficient of $O_2$ between water and hexadecane,[2] from which the free energy of transfer can be derived directly as

$$\Delta_{\mathrm{tr}}G(\mathrm{w} \rightarrow \mathrm{hex}) = -RT \ln K_P. \tag{1}$$

This provides a value of $-4.49$ kJ/mol at 298 K. Here $R$ is the ideal gas constant, $T$ is the temperature in K, and $K_P$ is the measured partition coefficient.

The free energy of transfer between two solvents can also be calculated from the difference between the corresponding free energies of solvation, provided that the appropriate standard states are used for the liquid phase. When comparing free energies of solvation, it is important to consider carefully the standard states, *i.e.*, the concentration scales. While for the gas phase the standard state of choice is always the ideal gas (typically with pressure $P^0 =$ 1 atm), for the liquid phase four different standard states have been used in the literature: the ideal dilute solution (also referred to as infinite dilution), unit molar concentration, unit molar fraction, and unit molal concentration. The theory linking standard free energies obtained with different standard states has been developed by Ben-Naim in the 1970s,[51] and is beautifully described in his textbook,[52] and discussed in recent reviews.[53,54] We summarize here briefly how free energy values are converted between different standard states, focusing on ideal dilute solutions (*i.e.*, "infinitely dilute" solutions), unit molar concentration and unit molar fraction. We refer to Ben-Naim's textbook[52] for the derivation of the equations that follow.

Free energies of transfer provide information on solute-solvent interactions, and on the preference of a certain solute for a solvent over another. Moeser *et al.*[54] explain that free energies of transfer "can be interpreted directly in terms of favorable or unfavorable solute-solvent interaction free energy" only for a transfer at constant molarity, *i.e.*, only if calculated as a difference between standard free energy of solvation at unit molar concentration. In fact, upon careful consideration of the theory,[51,52] we conclude that the same value of free energy of transfer is obtained for any transfer process not involving a change in the volume accessible to the solute. In particular, a transfer between two ideal dilute solutions also yields the same free energy of transfer, since in ideal dilute solutions the number density of the solute (*i.e.*, the number of solute molecules per unit volume) is by definition the same as in an ideal gas phase, and therefore is independent of the nature of the solute: For an ideal gas, we can apply the ideal gas law: $PV = nRT$. Hence, the number density of 1 mole of ideal gas is $\rho^g = n/V = P^0/RT$, with $P^0 = 1$ atm. On the other hand, free energies

of transfer should not be calculated as differences between free energies of solvation in the standard unit molar fraction, because the number density of the solute (and therefore, the volume accessible to the solute) would be different in the two solutions. Formally:

$$\Delta_{\rm tr}G(\mathrm{w} \rightarrow \mathrm{hex}) = \Delta G^{0\rho}_{\rm hex} - \Delta G^{0\rho}_{\rm w} = \Delta G^{0\mathrm{M}}_{\rm hex} - \Delta G^{0\mathrm{M}}_{\rm w} \neq \Delta G^{0x}_{\rm hex} - \Delta G^{0x}_{\rm w}. \tag{2}$$

Here the different superscripts indicate different standard states: $^{0\rho}$ for infinitely dilute (ideal) solutions, $^{0M}$ for unit molar concentrations, and $^{0x}$ for unit molar fractions. We can calculate the free energy of transfer for $O_2$ from water to hexadecane directly as the difference between the free energy of solvation at infinite dilution. At infinite dilution, the free energy of solvation $\Delta G^{0\rho}$ can be obtained from the unit-less Henry's law coefficients $H^{\rm cc}$ (also referred to as Ostwald coefficients[55]), measured from gas solubility in different solvents and available in the literature:

$$\Delta G^{0\rho} = -RT \ln(H^{\rm cc}). \tag{3}$$

For oxygen solubility into water and hexadecane the unitless Henry's law constants are 0.03178 and 0.2060,[56,57] respectively, which translate to solvation free energies of 8.55 kJ/mol and 3.92 kJ/mol, respectively. From these values of the free energy of solvation we can calculate directly the free energy of transfer as

$$\Delta_{\rm tr}G(\mathrm{w} \rightarrow \mathrm{hex}) = \Delta G^{0\rho}_{\rm hex} - \Delta G^{0\rho}_{\rm w}, \tag{4}$$

which provides a value of $(3.92 - 8.55)$ kJ/mol $= -4.63$ kJ/mol, similar to the value obtained from the partition coefficient between water and hexadecane ($-4.49$ kJ/mol).[2]

In addition to free energies of transfer, it is also informative to compare the free energies of solvation in water and hexadecane obtained in simulations and experiments. In simulations, free energies of solvation can be calculated using the thermodynamic integration

(TI) method.[58] As discussed above, free energies of solvation depend on the standard state considered for the process. Which standard state corresponds to the process simulated in TI calculations? An in-depth discussion on the correspondence between quantitities calculated in simulations and measured in experiments is reported by Shirts *et al.* in the appendix of ref. 59. Briefly, free energies of solvation obtained from TI simulations correspond to the transfer of one molecule of solute from an ideal gas phase to an ideal dilute solution, at constant temperature and pressure. In TI simulations, the volume of the gas phase and the liquid phase is (almost exactly) the same, *i.e.*, the number density of the solute is the same; hence, the free energy difference obtained from the simulation should be interpreted as the standard free energy of solvation obtained experimentally at infinite dilution ($\Delta G^{0\rho}$). Such free energies of solvation are not directly available for $O_2$ neither in water nor in hexadecane, but they can be derived using the theory by Ben-Naim.[51,52]

Abraham *et al.* reported free energies of solvation using unit mole fraction as a standard state.[60] The free energy of solvation at infinite dilution ($\Delta G^{0\rho}$) and at unit molar concentration ($\Delta G^{0\mathrm{M}}$) can be obtained from values at unit mole fraction ($\Delta G^{0x}$) by applying a correction to account for the different number density for the liquid phase in each standard state:

$$\Delta G^{0\mathrm{M}} = \Delta G^{0\rho} + RT \ln(\rho^l/\rho^g)_{\rho^l=1\mathrm{M}} \tag{5}$$

$$\Delta G^{0x} = \Delta G^{0\rho} + RT \ln(\rho^l/\rho^g)_{\rho^l=1x}, \tag{6}$$

where $\rho^l$ is the number density of the solute in the liquid phase (which depends on the standard state), and $\rho^g$ is the number density of the solute in the ideal gas phase.[52] If the unit molar (1 M) concentration is taken as the standard state for the liquid phase, the number density of the solute in the liquid phase, $\rho^l$, is $c^0 = 1$ mole/L; if unit molar fraction ($1\,x$) is taken as the standard state for the liquid phase, the number density of the solute in the liquid phase, $\rho^l$, is $c_{\mathrm{solvent}} = d_{\mathrm{solvent}}/MW_{\mathrm{solvent}}$ (where $d_{\mathrm{solvent}}$ is the density of the solvent and

$MW_{\rm solvent}$ is the molecular weight of the solvent). Notice that the standard state for the gas phase is, in all cases, the ideal gas, with pressure $P^0 = 1$ atm. Applying the ideal gas law: $PV = nRT$, we obtain (for 1 mole of ideal gas) a number density $\rho^g = n/V = P^0/RT$. Hence, the equations above can be written as:

$$\Delta G^{0\rm M} = \Delta G^{0\rho} + RT \ln(c^0 RT/P^0) \tag{7}$$

$$\Delta G^{0x} = \Delta G^{0\rho} + RT \ln(c_{\rm solvent} RT/P^0). \tag{8}$$

The free energy of hydration of $O_2$ in the standard unit molar fraction ($\Delta G_w^{0x}$) is available from ref. 60 and equals 26.48 kJ/mol; using the equations above, we derive the values for unit molar concentration and for infinite dilution:

$$\Delta G_{\rm w}^{0\rm M} = \Delta G_{\rm w}^{0x} - RT \ln c_{\rm w} = 16.52 \text{ kJ/mol}$$
$$\Delta G_{\rm w}^{0\rho} = \Delta G_{\rm w}^{0x} - RT \ln(c_{\rm w} RT/P^0) = 8.59 \text{ kJ/mol},$$

with the latter being very similar to the value obtained from Henry's law (8.55 kJ/mol).

The free energy of solvation of $O_2$ in hexadecane at infinite dilution can be derived in two ways: from the measured free energy of transfer from water to hexadecane, and from Henry's law (as described above). Using the value of $\Delta G_{\rm w}^{0\rho}$ obtained above and the experimental free energy of transfer[2] ($\Delta_{\rm tr} G = -4.49$ kJ/mol), we get:

$$\Delta G_{\rm hex}^{0\rho} = \Delta G_{\rm w}^{0\rho} + \Delta_{\rm tr} G = (8.59 - 4.49) = 4.10 \text{ kJ/mol},$$

in agreement with the value obtained from the unit-less Henry's constant[56,57] (3.92 kJ/mol).

# Methods

## Simulation setup and parameters

We calculated the properties of liquid $O_2$ from a number of models available in the literature, see Table 1. In all cases, we performed stochastic dynamics (SD) simulations of 2197 oxygen molecules at the boiling point (90.2 K) at atmospheric pressure. This corresponds to a simulation box of $(4.7\ \text{nm})^3$. We calculated electrostatic interactions with a real-space cut-off of 1 nm, using the PME algorithm[61,62] for long-range interactions, with a fourth order spline interpolation and a 0.12 nm grid spacing. Lennard-Jones (LJ) interactions used a 1 nm cut-off and the standard correction for long-range dispersion energy and pressure.[45] As shown by Shirts *et al.*,[63] the use of this analytical correction is appropriate for isotropic fluids even with heterogeneous Lennard-Jones sites, and makes thermodynamic properties substantially independent of the cut-off used for the calculation of non-bonded interactions.

For all SD simulations we used the leap-frog integrator with a time step of 1 fs and no constraints on bond lengths (when the harmonic force constant for the O–O bond was not available, we replaced it with a constraint.) To speed up the calculation of non-bonded interactions, we updated group-based neighbor lists (with a radius of 1 nm) every 10 steps. We used the Parrinello–Rahman barostat[64] with a time constant of 4 ps. Sampling was 5 ns in each simulation, and the last 4 ns were used for analysis. We extended the simulation time to 50 ns in one case, and observed virtually identical results (with reduced statistical uncertainties). We carried out all calculations using the GROMACS simulation package[65,66] (version 4.5.x–4.6.x).

The enthalpy of vaporization ($\Delta_{\text{vap}}H$) was calculated from simulations of pure oxygen in the liquid phase (at the boiling point, $T = 90.2$ K, $P = 1$ atm) and in the gas phase (at the same temperature). Considering ideal gas behavior of the gas phase and a small $PV$ term

for liquid, the enthalpy can be obtained from

$$\Delta_{\mathrm{vap}}H = U_{\mathrm{vapor}} - U_{\mathrm{liquid}} + RT. \tag{9}$$

The simulations of a single $O_2$ molecule in the gas phase were carried out for 50 ns in the NVT ensemble. Densities, internal energies, and their estimated uncertainties were calculated with GROMACS tools `g_energy` and `g_analyze`. The first 1 ns of simulation data was discarded from the analyses in all cases, and block averaging was employed to estimate the errors.

Oxygen diffusion coefficients $D$ were extracted from linear fits ($D = \mathrm{MSD}/(6\Delta)$) to the 3D mean squared displacement (MSD) data with the `g_msd` tool. Possible drift of the entire simulation cell was eliminated before the calculation. The fits were performed to the lag time ($\Delta$) interval between 1 ns and 5 ns. Error estimates were calculated as the difference values obtained from fits performed to lag time intervals 1–3 ns and 3–5 ns.

Additional tests evaluating the effects of long-range lattice summation for LJ interactions (PME-LJ)[67,68] and Verlet-type neighbor lists[69] were also performed. Furthermore, the performance of some CHARMM force field related models were evaluated using its native simulation parameters (see Results for details).

## Free energy calculations

We calculated the free energy of transfer for $O_2$ from water to hexadecane using Eq. (4), *i.e.*, as a difference of the free energies of hydration and solvation into hexadecane. These terms were calculated using the thermodynamic integration (TI) method.[58] In TI calculations, interactions between oxygen and the solvent molecules are scaled by a coupling parameter $\lambda$ in the interval $[0, 1]$; $\lambda = 1$ corresponds to the full solute-solvent interaction, which is the coupled (solvated) state, while $\lambda = 0$ corresponds to the absence of interactions between solute and solvent, which is the decoupled state. Intramolecular interactions are not decoupled.

The free energy difference $\Delta G$ between the coupled and decoupled states equals

$$\Delta G = \int_0^1 \langle \partial \mathcal{H}(\lambda)/\partial\lambda \rangle_\lambda \, \mathrm{d}\lambda, \tag{10}$$

where $\mathcal{H}$ the Hamiltonian of the system; angle brackets indicate that averaging is performed at each $\lambda$ value.

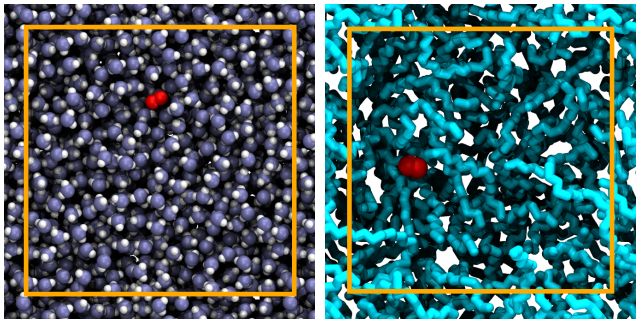

Figure 1: Snapshots of the systems employed in the TI calculations: Left: $O_2$ (red) among 1728 water molecules (blue and white). Right: $O_2$ among 108 hexadecane molecules (cyan). Both systems are of similar size $(3.7\ \mathrm{nm})^3$. Simulation box borders (with periodic boundary conditions) are drawn in orange.

To improve the precision of the TI calculations we performed two separate sets of simulations, decoupling separately the Coulomb contribution and the Lennard-Jones contribution to the free energy of solvation, as suggested by Boresch.[70] A total of 23 $\lambda$ values (0.00, 0.03, 0.09, 0.14, 0.18, 0.24, 0.30, 0.35, 0.40, 0.45, 0.48, 0.52, 0.55, 0.58, 0.60, 0.62, 0.65, 0.70, 0.75, 0.80, 0.85, 0.90, and 1.00) were employed in both sets of simulations for each oxygen model and for each solvent. To avoid singularities in the potential when interactions are turned off, we used a soft-core potential for non-bonded interactions.[71] We set the soft-core parameter $\alpha$ to 0.65, the soft-core power to 1, and the soft-core $\sigma$ to 0.30. In all simulations, the temperature was 298 K. All other simulation parameters were identical to the ones used in simulations of liquid oxygen.

In all TI calculations, a single oxygen molecule was solvated in a box of solvent. The water phase was modelled with a cubic box filled with 1728 SPC[72] water molecules (size of

3.7 $nm^3$), see the left panel of Fig. 1. For hexadecane, we used a box of equal size filled with 108 molecules (right panel in Fig. 1). The alkane was described with the parameters of Berger united atom lipid tails.[73] In some cases (see Results below) we performed additional simulations using the TIP3P water model[74] and all-atom models for hexadecane: the Slipids model,[75] and the OPLS-AA compatible model.[76] The results for some models associated with the CHARMM force field were further verified by repeating the simulations using the CHARMM-compatible models for water[48] and hexadecane,[77] the Lorentz–Berthelot combination rules, as well as the native simulation parameters of the CHARMM force field[78] (see Results for details).

In all cases, constraints were not used whenever information on the bond force constant was available (see Table 1 for details). Simulations were performed at 298 K employing the stochastic dynamics (SD) integrator with a time step of 1 fs, for a total sampling of 20 ns per window, out of which the first 1 ns was discarded.

# Results and discussion

We calculated four different thermodynamic properties (density, heat of vaporization, free energy of hydration, and free energy of solvation in hexadecane) for 14 different models of $O_2$ available in the literature (see Table 1). Before describing the results obtained with each model, we introduce below the different models and summarize their main features.

The models differ essentially in the target properties used during the parameterization. Some of the models are based on target properties derived from calculations: the second virial coefficients (Bouanich[13]), the vapor pressure and bubble density (Bohn[15]), or volumes at zero pressure (Fischer[10,80]). Other models are optimized to reproduce measured thermodynamic properties such as the vapour–liquid coexistence curves in Monte Carlo simulations (Hansen-QR[17] and Zhang-QR[79]). Several models in the literature are supposedly compatible with the CHARMM force field. In general, they are not based on reproducing thermodynamic

**Table 1: $O_2$ models evaluated in the present study. The Lennard-Jones parameters ($\epsilon$ and $\sigma$) are reported, together with bond lengths ($d$) and the charges in models with a dipole (CHARMM-D) or a quadrupole moment (CHARMM-QR, Hansen-QR, Zhang-QR, QS, QL). Finally, if the information on the force constant $k_r$ of the O–O bond is available, it is given; otherwise the O–O distance is constrained. The model used in ref. 36 also contains a quadrupole moment but the charges are not stated in the publication.**

| Earlier models (used in) | $\epsilon$ (kJ/mol) | $\sigma$ (nm) | $d$ (nm) | $q_O(q_{VS})$ (e) | $k_r$ (kJ/mol/nm) |
|---|---|---|---|---|---|
| CHARMM[48] ([19,20,22,23]) | 0.5021 | 0.3029 | 0.1208 | 0 | constraint |
| CHARMM-2[48] ([9,35]) | 0.5021 | 0.3029 | 0.112 | 0 | constraint |
| CHARMM-B (bond)[8] | 0.5021 | 0.3029 | 0.1208 | 0 | 708770 |
| CHARMM-QR[11] ([37]) | 0.5021 | 0.3029 | 0.123 | -0.1114 (0.2228) | 251208 |
| CHARMM-QR2[11] | 0.5021 | 0.3029 | 0.123 | -0.226 (0.452) | 251208 |
| CHARMM-D[48] ([9,35]) | 0.6364 | 0.3151 | 0.116 | $\pm$0.021 | constraint |
| Fischer[10] ([18,24]) | 0.363 | 0.309 | 0.1016 | 0 | constraint |
| Victor[12] ([25,30]) | 0.557 | 0.357 | 0.1214 | 0 | constraint |
| Cordeiro (bond)[16] | 0.291 | 0.26 | 0.121 | 0 | $1.66 \times 10^7$ |
| Cordeiro (constraint)[16] | 0.291 | 0.26 | 0.121 | 0 | constraint |
| Porrini[14] | 0.4351 | 0.296 | 0.112 | 0 | constraint |
| Bouanich[13] ([36]) | 0.4372 | 0.30058 | 0.121 | 0 | constraint |
| Bohn[15] | 0.316 | 0.32104 | 0.07063 | 0 | constraint |
| Hansen-QR[17] | 0.4078 | 0.3013 | 0.121 | -0.123 (0.246) | constraint |
| Zhang-QR[79] | 0.4074 | 0.302 | 0.121 | -0.113 (0.226) | constraint |
| Models developed in this work | | | | | |
| noQ | 0.4029 | 0.313 | 0.1016 | 0 | constraint |
| QS | 0.4469 | 0.3044 | 0.123 | -0.1114 (0.2228) | 251208 |
| QL | 0.4451 | 0.3044 | 0.123 | -0.226 (0.452) | 251208 |

properties of $O_2$ as they use LJ parameters from carbonyl groups of proteins.[48] Models exist with two different bond lengths (CHARMM and CHARMM-2) to be used with constraints or a harmonic bond (CHARMM-B[8]). The same models have been modified to contain a quadrupole moment (CHARMM-QR[11] and CHARMM-QR2)). The hydration free energy of the CHARMM-QR model was also calculated in a subsequent study,[37] but not used to optimize the model. Heme oxygen parameters from CHARMM containing a dipole moment have also been developed (CHARMM-D, from the Supplementary Information of Wang *et al.*[35]). Some of the models considered here were optimized to reproduce the solvation free energies in MD. The model by Cordeiro[16] considered solvation free energies into both water and cyclohexane, while the one by Victor[12] is based solely on the free energy of hydration. In the case of the model by Porrini *et al.*,[14] the source of the LJ parameters is not stated in the paper, yet their values appear to be derived from carbonyl oxygen in the OPLS force field (with scaling of $\epsilon$ by 1/2). Since the choice of simulation parameters affects the performance of the models, we have briefly described the original simulation setups in the Supporting Information.

Four of the selected models have a quadrupole moment, while the other ten models do not. Models with a quadrupole moment consist of 3 interaction sites shown in Fig. 2: two interaction sites (with both Lennard-Jones and Coulomb interactions) are located on oxygen nuclei, and a third, massless interaction site (with Coulomb interaction only) is located halfway between the oxygens. The models featuring a quadrupole moment have different partial charges and quadrupole moments. Also, bond length and Lennard-Jones parameters are different. The main parameters in each model are listed in Table 1.

The density experimentally measured for liquid oxygen at its boiling point (90.2 K) is 1141 kg/m$^3$,[81] and the heat of vaporization is 6.82 kJ/mol.[81] Table 2 shows that, using the simulation parameters detailed above, most models reproduce experimental densities within about 5% error.

Also, most models overestimate the density of liquid $O_2$. Models showing larger discrep-

ancies with experiments include the original and modified CHARMM parameters[8,9,11,35,48] as well as the models by Victor[12] and Porrini.[14] When comparing results on the heat of vaporization, errors are generally larger: only two models show errors below 10%. Some models overestimate and others underestimate the measured quantity.

None of the CHARMM-compatible models tested here reproduces quantitatively experimentally measured $O_2$ density and heat of vaporization. We notice that all the parameters modified in the six different models analyzed here (namely the O–O bond length, the use of constraints, the presence of a quadrupole or a dipole moment) affect the thermodynamic properties. The effect is minor for the use of constraints (with the exception of the heat of vaporization, which is significantly affected by the use of constraints, as expected), but significant for bond length and partial charges. CHARMM-compatible models with a quadrupole moment (CHARMM-QR[11] and CHARMM-QR2) show better agreement with experimental density (error of $\sim$3%), yet the heats of vaporization are still off by more than 10%. We hypothesized that the discrepancies may be due to the use of a long-range dispersion correction to virtually eliminate cut-off effects[59] (in simulations with CHARMM force fields a cut-off of 1.2 nm with shift function is generally used instead). To test this hypothesis, we evaluated the performance for three different CHARMM-based models (see Table 2) using standard CHARMM simulation parameters provided by the CHARMM-GUI input generator for GROMACS[78] (including the Verlet-list based cut-off scheme), and the GROMACS version 5.0.x[82] (except for the SD integrator and the time step of 1 fs). This improves the results only slightly (see Table 2), bringing the value of density to within 5% of its experimental value. However, the heat of vaporization is still off by 13% and 12% for models without and with the QR moment, respectively.

In conclusion, none of the models tested here reproduces quantitatively the density and the heat of vaporization of $O_2$. Models with smaller errors in one of the two thermodynamic metrics typically show larger errors in the other metric.

We now compare simulations and experiments in terms of free energies of solvation and

**Table 2: Densities ($\rho$) and heats of vaporization ($\Delta_{\mathrm{vap}}H$) calculated for earlier models as well as those developed here for $O_2$. Values of density ($\rho$) are given in kg/m$^3$, whereas the heats of vaporization ($\Delta_{\mathrm{vap}}H$) are given in kJ/mol. Errors are calculated using block averaging. The error estimates for $\Delta_{\mathrm{vap}}H$, calculated as $\delta U_{\mathrm{liquid}}+\delta U_{\mathrm{gas}}$, are equal to or smaller than 0.01 kJ/mol and therefore not listed. Simulations with the model by Cordeiro[16] with a harmonic bond were unstable, so they were run with a constraint instead. Simulations run with CHARMM-compatible simulation parameters and GROMACS 5 are marked with $^*$.**

| Earlier models (used in) | $\rho$ | $\Delta_{\mathrm{vap}}H$ |
|---|---|---|
| CHARMM[48] ([8,19,20,22,23]) | 1209.9±0.1 | 8.16 |
| CHARMM$^*$[48] ([19,20,22,23]) | 1189.7±0.1 | 7.71 |
| CHARMM-2[48] ([9,35]) | 1259.7±0.1 | 8.60 |
| CHARMM-B (bond)[8] | 1218.9±0.1 | 8.21 |
| CHARMM-QR[11] ([37]) | 1198.7±0.1 | 8.07 |
| CHARMM-QR2[11] ([37]) | 1198.7±0.1 | 8.07 |
| CHARMM-QR$^*$[11] ([37]) | 1178.6±0.1 | 7.62 |
| CHARMM-QR2$^*$[11] ([37]) | 1180.8±0.1 | 7.65 |
| CHARMM-D[48] ([9,35]) | 1255.6±0.1 | 12.78 |
| Fischer[10] ([18,24]) | 1132.7±0.1 | 5.75 |
| Victor[12] ([25,30]) | 822.8±0.1 | 10.42 |
| Cordeiro (constraint)[16] | 1147.4±1.1 | 2.43 |
| Porrini[14] | 1276.5±0.2 | 6.88 |
| Bouanich[13] ([36]) | 1178.2±0.2 | 6.62 |
| Bohn[15] | 1145.2±0.1 | 5.90 |
| Hansen-QR[17] | 1128.4±0.2 | 5.12 |
| Zhang-QR[79] | 1122.0±0.2 | 5.12 |
| Models developed in this work | | |
| noQ | 1141.0±0.2 | 6.82 |
| QS | 1140.7±0.1 | 6.82 |
| QL | 1141.1±0.2 | 6.82 |
| noQ (LJ-PME) | 1140.7±0.1 | 6.82 |
| noQ (Verlet list) | 1140.6±0.2 | 6.82 |
| QS (Verlet list) | 1141.7±0.1 | 6.84 |
| Experiment | 1141[81] | 6.82[81] |

transfer. First of all, as shown in Table 3, all 14 models overestimate the free energy of transfer, showing too favorable transfer from water to hexadecane, with errors larger than 2 kJ/mol (*i.e.*, about 50% of the experimental value) in almost all cases. The average error over the 14 models is 2.8 kJ/mol, corresponding to 62% of the experimental value. Smaller errors are shown only by the models of Cordeiro[16] and CHARMM-D[9,31,35] (which has a permanent dipole moment, hence it is only suitable for use in Hemes or other particular cases). Second, errors in the free energy of hydration are generally smaller than errors in the free energy of solvation in hexadecane; most models show errors smaller than 1 kJ/mol in the free energy of hydration, while all models (with the exception of the one by Cordeiro[16]) show errors larger than 1 kJ/mol in the free energy of solvation in hexadecane; in other words, most of the error in the free energy of transfer comes from an incorrect estimation of solvation in the alkane, not in water.

In the case of CHARMM-based models, again, discrepancies could be due to our use of simulation parameters and methods different from the CHARMM default parameters, namely: (1) the use of a long-range correction for LJ interactions; (2) the use of geometric combination rules (instead of Lorentz–Berthelot); (3) the use of models for water and hexadecane not taken from the CHARMM force field. To better understand the origin of the discrepancies with experiments, we repeated the calculations with the original CHARMM model as well as the quadrupole moment containing ones (CHARMM-QR and CHARMM-QR2) using the appropriate CHARMM all-atom models for hexadecane[77] and water (the special CHARMM TIP3P, sometimes referred to as TIPS3P[48]), a cut-off of 1.2 nm for non-bonded interactions with shift function and no long-range dispersion correction, as normally used in simulations with the CHARMM force field. The simulation parameters were downloaded for GROMACS from the CHARMM-GUI website.[78] The use of native parameters and models improves the solvation free energies of the CHARMM model (particularly the free energy of hydration) but the free energy of solvation in hexadenane is still off by 2.5 kJ/mol or more. This also holds true for the CHARMM-based models containing a quadrupole

**Table 3: Hydration free energies ($\Delta G_{\mathrm{wat}}$) and free energies of solvation into hexadecane ($\Delta G_{\mathrm{hd}}$)) as well as the free energies of transfer ($\Delta_{\mathrm{tr}}G$) calculated for the derived models and the earlier models for $O_2$. Values are given in kJ/mol. Simulations run with CHARMM-compatible simulation parameters and GROMACS 5 are marked with $^*$.**

| Earlier models (used in) | $\Delta G_{\mathrm{hd}}$ | $\Delta G_{\mathrm{wat}}$ | $\Delta_{\mathrm{tr}}G$ |
|---|---|---|---|
| CHARMM[48] ([8,19,20,22,23]) | 0.84±0.02 | 9.13±0.02 | 8.30±0.04 |
| CHARMM*[48] ([19,20,22,23]) | 1.39±0.03 | 8.46±0.02 | 7.07±0.05 |
| CHARMM-2[48] ([9,35]) | 0.45±0.02 | 8.66±0.02 | 8.22±0.04 |
| CHARMM-B (bond)[8] | 0.82±0.02 | 9.12±0.02 | 8.30±0.04 |
| CHARMM-QR[11] ([37]) | 0.93±0.02 | 9.13±0.03 | 8.20±0.05 |
| CHARMM-QR2[11] ([37]) | 0.95±0.02 | 8.86±0.04 | 7.91±0.06 |
| CHARMM-QR*[11] ([37]) | 1.46±0.03 | 8.49±0.02 | 7.04±0.05 |
| CHARMM-QR2*[11] ([37]) | 1.43±0.03 | 8.21±0.04 | 6.78±0.07 |
| CHARMM-D[48] ([9,35]) | 1.35±0.02 | 7.77±0.03 | 6.42±0.05 |
| Fischer[10] ([18,24]) | 2.47±0.02 | 10.19±0.02 | 7.72±0.04 |
| Victor[12] ([25,30]) | 0.27±0.03 | 9.13±0.03 | 8.86±0.05 |
| Cordeiro (constraint)[16] | 3.28±0.02 | 9.39±0.02 | 6.10±0.04 |
| Porrini[14] | 1.46±0.02 | 9.12±0.02 | 7.66±0.04 |
| Bouanich[13] ([36]) | 1.83±0.02 | 9.83±0.02 | 8.00±0.04 |
| Bohn[15] | 2.30±0.02 | 9.85±0.03 | 7.54±0.05 |
| Hansen-QR[17] | 2.34±0.02 | 10.09±0.03 | 7.76±0.05 |
| Zhang-QR[79] | 2.33±0.02 | 10.17±0.03 | 7.84±0.05 |
| Models developed in this work | | | |
| noQ | 1.81±0.02 | 8.47±0.02 | 6.66±0.04 |
| QS | 1.85±0.02 | 8.58±0.03 | 6.73±0.05 |
| QL | 1.87±0.02 | 9.70±0.04 | 7.83±0.06 |
| QS (Verlet list) | 1.95±0.02 | 8.50±0.03 | 6.55±0.05 |
| QS w/ Slipids[75] | 1.91±0.03 | 8.58±0.03 | 6.67±0.05 |
| QS w/ OPLS-AA[76] | 1.54±0.03 | 8.58±0.03 | 7.04±0.06 |
| QS w/ TIP3P[74] | 1.85±0.02 | 8.83±0.03 | 6.98±0.05 |
| Experiment | 3.92[57] | 8.55–8.59[12,56,83] | 4.49–4.63[60,84] |

moment.

The results above indicate that there is room for improvement of the $O_2$ models, so we set out to optimize models with and without a quadrupole moment. In the parameterization, we used the density of pure liquid $O_2$ and its heat of vaporization as target properties, as routinely done in the parameterization of atomistic force fields for liquids and biological macromolecules. We used free energies of solvation only to validate the models, because using them as targets in the parameterization would have implied a dependence of our $O_2$ models on the specific force field for the solvent, potentially limiting the transferability of the models. For the development of the new models, we used two different starting points: for the charge–free model, we used bonded interactions from the model by Fischer and Lago[10] ("Fischer" in Tables 1, 2, and 3), containing two uncharged particles separated by a (fixed) bond of 0.1016 nm; this model has been employed in studies on $O_2$ permeation through lipid bilayers.[18,24] For the model with a quadrupole moment, we used charges and bonded interactions from Hub *et al.*[11] (CHARMM-QR). This model has been employed in studies on gas–protein interactions[37] and protein-assisted gas permeation.[11]

The experimentally measured values $Q_{\mathrm{exp}}$ and the quadrupole tensor components are related by $Q^2_{\mathrm{exp}} = 2/3 \times (Q^2_{xx} + Q^2_{yy} + Q^2_{zz})$, which, for the case of $O_2$ ($Q_{zz} = 2Q_{xx} = 2Q_{yy}$), reduces to $Q_{\mathrm{exp}} = Q_{zz}$.[85] Using *ab initio* calculations at the MP2 level to evaluate the quadrupole moment,[11] Hub *et al.* obtained a value of $Q_{zz} = 0.82$ DÅ. If we evaluate the quadrupole moment using the following equation: $Q_{zz} = 1/2qd^2$, we notice that the charges used in the model of Hub *et al.* (see Table 1 and Figure 2) only produce a value of $Q_{zz} = 0.40$ DÅ. Such value has actually been measured experimentally.[86,87] Hence we decided to test two different sets of partial charges, producing two different values of the quadrupole moment: the partial charges reproducing the experimental value of the quadrupole moment and those reproducing the value of quadrupole moment calculated *ab initio* by Hub *et al.* (see Table 1). We also evaluated the performance of the model by Hub *et al.* with the larger quadrupole moment (as quoted by[44]). In total, we optimized three models of $O_2$: one with

no quadrupole (noQ), one with a smaller quadrupole moment (QS), and one with a larger quadrupole moment (QL). For each model, we systematically varied the Lennard-Jones (LJ) parameters of the oxygen atom. Dozens of $(\epsilon, \sigma)$ pairs were considered for each of the three new models, until we obtained good agreement with experiments on both density and heat of vaporization at the boiling point (error below 0.1%).

After optimization of the LJ parameters, all three models reproduce very well both density and heat of vaporization, independently of the presence and the value of the quadrupole moment (see Table 2). Repeating the simulations with different cut-off schemes, namely the group scheme and the Verlet scheme[69] (default in GROMACS v5.0.x and later), and using the PME method to evaluate the long-range Lennard-Jones interactions[67,68] provided virtually identical results within statistical uncertainty (see Table 2). We notice that both density and heat of vaporization obtained with our model are independent of the LJ cut-off, as long as a correction for long-range dispersion interactions (or alternatively the LJ-PME method) is used — in agreement with observations by Shirts *et al.*[63]

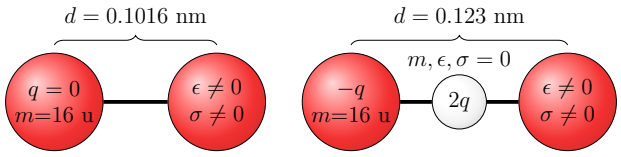


Figure 2: Two templates used for parameterization. Left: noQ model, without charges and with bonded parameters from ref. 10. Right: QL and QS models have a charged dummy particle in between the oxygen nuclei. The bonded interactions are taken from ref. 11, and the values of partial charges depend on the size of the quadrupole moment. For QL, $q = 0.226$ e[44] and for QS, $q = 0.11136$ e.[11] All existing models evaluated earlier containing a quadrupole moment have this linear structure with different values for $d, \epsilon, \sigma$, and $q$.

We then calculated the free energies of solvating $O_2$ into water and hexadecane, as well as the free energy of transfer for $O_2$ from water to hexadecane, for the newly developed models. The results (see Table 3) show that two of our models, the one with no quadrupole (noQ) and the one with the smaller quadrupole moment (QS), reproduce very well the experimental free energy of hydration, with deviations below 1% from the experimental values. The

model with the larger quadrupole (QL), instead, clearly overestimates the free energy of hydration, showing a deviation of 1.15 kJ/mol from the experimental value – larger than the error obtained with most other models tested here. All three models underestimate the free energy of solvation in hexadecane; compared to experiments, the error is about 2 kJ/mol for all of our models, comparable to the error obtained by most other models. As for densities and heat of vaporization, the use of Verlet-type neighbor lists (instead of the group based ones) has a minor effect on all results (see Table 3).

Considering free energies of transfer, our models with no quadrupole moment (noQ) and with a small quadrupole moment (QS) perform better than other models with reasonable density and heat of vaporization. The CHARMM and CHARMM-QR models perform almost equally well when simulated with native CHARMM simulation parameters and models, despite the significant errors in densities and heat of vaporization. We also notice that the computational cost of all-atom simulations is between 5 and 10 times higher compared to united-atom models (with and without GPU, respectively; for the comparison we used the same hardware and the same version of the software, GROMACS v5.0.7). The quality of the models, both existing ones and those developed here, is summarized in Figure 3. The figure shows the relative errors (with respect to the experimental values) of the four metrics used in the parameterization and validation of the models. The noQ and QS models show the smallest deviations from experimental values, but they cannot properly capture the free energy of solvation into hexadecane.

To better understand the reasons for the mismatch between simulation models and experiments, in terms of free energy of solvation in hexadecane, we tested our QS model (with a smaller quadrupole moment) with two all-atom alkane force fields: the alkane model from Slipids[75] and a modified OPLS-AA model by Maciejewski *et al.*[76] These contain partial charges either on all carbon and hydrogen atoms (OPLS-AA) or on the terminal methyl groups (Slipids). By virtue of the presence of partial charges, their interaction with our QS model is different from the interaction between united-atom alkanes and QS model:

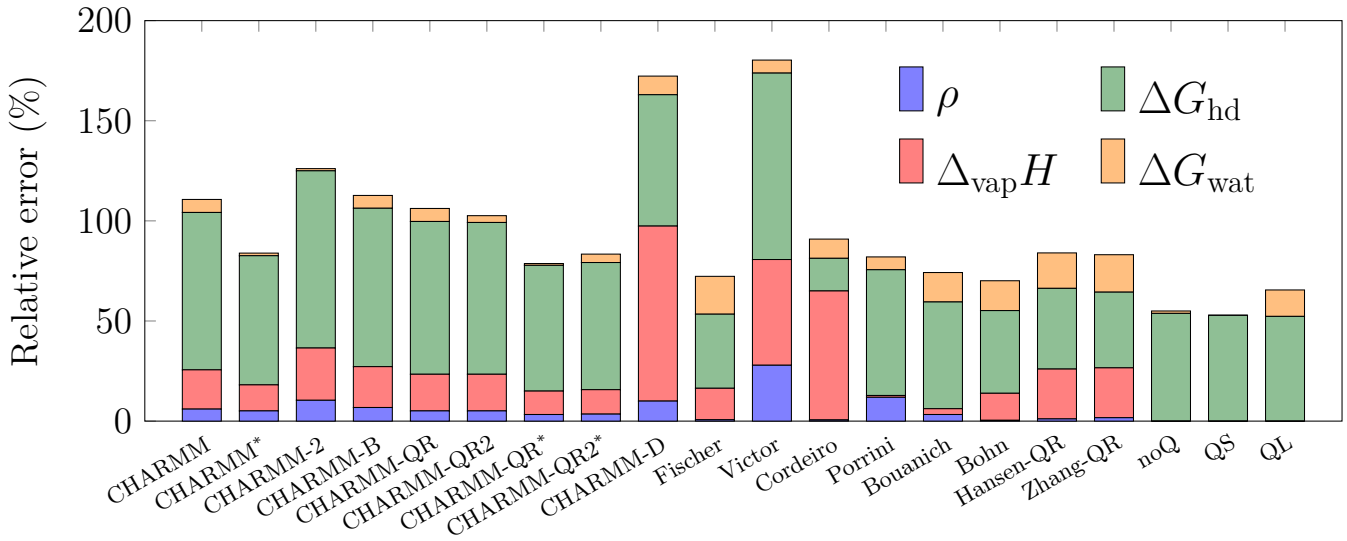


Figure 3: Summary of the quality of both the existing models and the models developed in this work. The bars show relative errors with respect to experimental values given in Tables 2 and 3.

dipole-quadrupole interactions are taken into account in the case of all-atom alkanes, not with united-atom alkanes. Surprisingly, differences in the free energy of solvation of $O_2$ in hexadecane are minor (see Table 3). The small effect of alkane partial charges on the free energy of solvation of $O_2$ parallels the very minor difference between united-atom and all-atom alkane models in terms of dielectric constant: according to Vorobyov *et al.*, the CHARMM all-atom model for decane yields a dielectric constant of 1.02, extremely close to the constant obtained from models with no partial charges (1) and very far from both the experimental value (1.98) and the value obtained with the CHARMM polarizable model (2.07–2.12).[88] It is well known that hydrocarbons are highly polarizable molecules, and their polarizability increases with their size.[89] Also, the polarizability of hydrocarbons is significantly higher than the polarizability of water and other polar liquids.[89] We hypothesize that, for the case of $O_2$ in hydrocarbons (and possibly other non-polar solvents), polarizability plays an important role in solute-solvent interactions and the free energy of solvation.

Finally, a proper oxygen model should also perform well in terms of dynamic properties that are relevant for numerous applications such as membrane permeation[43] and diffusion

to protein binding sites.[44] To ensure this, we calculated the diffusion coefficients of a single oxygen molecule in water and in hexadecane at 298 K from the systems employed in the TI simulations. The diffusion coefficient values, given in Table 4, show good agreement with experiment in the case of hexadecane, while the diffusion coefficients calculated for oxygen in water are overestimated by at least 50%. However, this discrepancy likely arises from the quality of the employed water models; both SPC and TIP3P are known to substantially overestimate the diffusion coefficient of water.[90] Furthermore, the error estimates of these diffusion coefficients are fairly large due to the limited statistics provided by a single diffusing oxygen molecule.

**Table 4: Diffusion coefficients of oxygen in water (SPC) and hexadecane (Berger), given in cm$^2$/s. Values with other models are labeled as follows: *a*: with TIP3P, *b*: with OPLS-AA, *c*: with Slipids. "Exp." stands for experimental values.**

| Model | $10^5 \times D_{\text{water}}$ | $10^5 \times D_{\text{hexadecane}}$ |
|---|---|---|
| noQ | 3.23±0.16 | 2.26±0.23 |
| QS | 5.06±2.51<br>5.11±3.16$^a$ | 2.47±0.33<br>4.65±0.19$^b$<br>2.25±0.28$^c$ |
| QL | 3.55±0.62 | 2.30±1.61 |
| Exp. | 1.96[91] | 2.5–2.7[92,93] |

# Conclusions

In the present work we verified the performance of 14 different models of $O_2$ available in the literature by calculating densities, heats of vaporization, and free energies of solvation in water and hexadecane. Comparison with experimental data shows significant differences among the models, and most importantly all of them fail to reproduce quantitatively measured thermodynamic quantities. We also optimized new $O_2$ models, with and without a quadrupole moment. Both of the new models show major improvements over previous models in terms

of thermodynamic properties and very good agreement with experimental measures, with the exception of the free energy of solvation in hexadecane. Older models also yield similar or larger errors on the free energy of solvation in hexadecane.

While the key conclusions of our work may sound critical, some of the tested $O_2$ models (and in particular the new models developed in this work) predict the correct physical trends, and the agreement with experimental data is reasonably good. Yet, the results shown in this work suggest that current pairwise-additive models are not adequate to accurately describe the thermodynamics of solvation of non-polar species in non-polar media (including more biologically relevant ones, such as lipid bilayers). For such cases, an explicit treatment of electronic polarizability is probably necessary.[88]

## Acknowledgement

We thank CSC – IT Center for Science (Espoo, Finland) and GENCI-CINES (France, grant c2016076353) for computing resources. LM thanks Michael H. Abraham for fruitful discussions on free energies of solvation and standard states. LM acknowledges funding from the Institut national de la santé et de la recherche médicale (INSERM). MJ and IV thank the Academy of Finland (Centre of Excellence program) and the European Research Council (Advanced Grant CROWDED-PRO-LIPIDS) for financial support.

## References

(1) Battino, R.; Evans, F. D.; Danforth, W. F. Solubilities of 7 Gases in Olive Oil With Reference to Theories of Transport Through Cell Membrane. *Journal of the American Oil Chemists Society* **1968**, *45*, 830–833.

(2) Abraham, M.; Grellier, P.; McGill, R. Determination of Olive Oil–Gas and Hexadecane–Gas Partition Coefficients, and Calculation of the Corresponding Olive Oil–Water

and Hexadecane–Water Partition Coefficients. *Journal of the Chemical Society, Perkin Transactions 2* **1987**, 797–803.

(3) Subczynski, W.; Hyde, J.; Kusumi, A. Oxygen Permeability of Phosphatidylcholine–Cholesterol Membranes. *Proceedings of the National Academy of Sciences of the United States of America* **1989**, *86*, 4474.

(4) Altenbach, C.; Greenhalgh, D. A.; Khorana, H. G.; Hubbell, W. L. A Collision Gradient Method to Determine the Immersion Depth of Nitroxides in Lipid Bilayers: Application to Spin-Labeled Mutants of Bacteriorhodopsin. *Proceedings of the National Academy of Sciences of the United States of America* **1994**, *91*, 1667–71.

(5) Perozo, E.; Cortes, D. M.; Cuello, L. G. Three-Dimensional Architecture and Gating Mechanism of a K+ Channel Studied by EPR Spectroscopy. *Nature Structural Biology* **1998**, *5*, 459–69.

(6) Nielsen, R. D.; Che, K.; Gelb, M. H.; Robinson, B. H. A Ruler for Determining the Position of Proteins in Membranes. *Journal of the American Chemical Society* **2005**, *127*, 6430–6442.

(7) Evanics, F.; Hwang, P. M.; Cheng, Y.; Kay, L. E.; Prosser, R. S. Topology of an Outer-Membrane Enzyme: Measuring Oxygen and Water Contacts in Solution NMR Studies of PagP. *Journal of the American Chemical Society* **2006**, *128*, 8256–8264.

(8) Holland, B. W.; Berry, M. D.; Gray, C.; Tomberli, B. A Permeability Study of $O_2$ and the Trace Amine P-Tyramine Through Model Phosphatidylcholine Bilayers. *PLoS One* **2015**, *10*, e0122468.

(9) Cohen, J.; Arkhipov, A.; Braun, R.; Schulten, K. Imaging the Migration Pathways for $O_2$, CO, NO, and Xe Inside Myoglobin. *Biophysical Journal* **2006**, *91*, 1844–1857.

(10) Fischer, J.; Lago, S. Thermodynamic Perturbation Theory for Molecular Liquid Mixtures. *The Journal of Chemical Physics* **1983**, *78*, 5750.

(11) Hub, J.; de Groot, B. Mechanism of Selectivity in Aquaporins and Aquaglyceroporins. *Proceedings of the National Academy of Sciences of the United States of America* **2008**, *105*, 1198.

(12) Victor, B. L.; Baptista, A. M.; Soares, C. M. Dioxygen and Nitric Oxide Pathways and Affinity to the Catalytic Site of Rubredoxin: Oxygen Oxidoreductase From Desulfovibrio Gigas. *JBIC Journal of Biological Inorganic Chemistry* **2009**, *14*, 853–862.

(13) Bouanich, J.-P. Site-Site Lennard-Jones Potential Parameters for $N_2$, $O_2$, $H_2$, CO and $CO_2$. *Journal of Quantitative Spectroscopy and Radiative Transfer* **1992**, *47*, 243–250.

(14) Porrini, M.; Daskalakis, V.; Farantos, S. C. Exploring the Topography of Free Energy Surfaces and Kinetics of Cytochrome C Oxidases Interacting With Small Ligands. *RSC Advances* **2012**, *2*, 5828–5836.

(15) Bohn, M.; Lustig, R.; Fischer, J. Description of Polyatomic Real Substances by Two-Center Lennard-Jones Model Fluids. *Fluid Phase Equilibria* **1986**, *25*, 251–262.

(16) Cordeiro, R. M. Reactive Oxygen Species at Phospholipid Bilayers: Distribution, Mobility and Permeation. *Biochimica et Biophysica Acta (BBA) - Biomembranes* **2014**, *1838*, 438–444.

(17) Hansen, N.; Agbor, F. A.; Keil, F. J. New Force Fields for Nitrous Oxide and Oxygen and Their Application to Phase Equilibria Simulations. *Fluid Phase Equilibria* **2007**, *259*, 180–188.

(18) Marrink, S.; Berendsen, H. Permeation Process of Small Molecules Across Lipid Membranes Studied by Molecular Dynamics Simulations. *The Journal of Physical Chemistry* **1996**, *100*, 16729–16738.

(19) Jedlovszky, P.; Mezei, M. Calculation of the Free Energy Profile of $H_2O$, $O_2$, CO, $CO_2$, NO, and $CHCl_3$ in a Lipid Bilayer With a Cavity Insertion Variant of the Widom Method. *Journal of the American Chemical Society* **2000**, *122*, 5125–5131.

(20) Jedlovszky, P.; Mezei, M. Effect of Cholesterol on the Properties of Phospholipid Membranes. 2. Free Energy Profile of Small Molecules. *The Journal of Physical Chemistry B* **2003**, *107*, 5322–5332.

(21) Yuan, H.; Jameson, C. J.; Murad, S. Exploring Gas Permeability of Lipid Membranes Using Coarse-Grained Molecular Dynamics. *Molecular Simulation* **2009**, *35*, 953–961.

(22) Shinoda, W.; Mikami, M.; Baba, T.; Hato, M. Molecular Dynamics Study on the Effects of Chain Branching on the Physical Properties of Lipid Bilayers: 2. Permeability. *The Journal of Physical Chemistry B* **2004**, *108*, 9346–9356.

(23) Shinoda, K.; Shinoda, W.; Baba, T.; Mikami, M. Comparative Molecular Dynamics Study of Ether-And Ester-Linked Phospholipid Bilayers. *The Journal of Chemical Physics* **2004**, *121*, 9648–9654.

(24) Sugii, T.; Takagi, S.; Matsumoto, Y. A Molecular-Dynamics Study of Lipid Bilayers: Effects of the Hydrocarbon Chain Length on Permeability. *The Journal of Chemical Physics* **2005**, *123*, 184714.

(25) Damas, J. M.; Baptista, A. M.; Soares, C. M. The Pathway for $O_2$ Diffusion Inside CotA Laccase and Possible Implications on the Multicopper Oxidases Family. *Journal of Chemical Theory and Computation* **2014**, *10*, 3525–3531.

(26) Cohen, J.; Kim, K.; Posewitz, M.; Ghirardi, M. L.; Schulten, K.; Seibert, M.; King, P. Molecular Dynamics and Experimental Investigation of $H_2$ and $O_2$ Diffusion in [Fe]-Hydrogenase. *Biochemical Society Transactions* **2005**, *33*, 80–82.

(27) Johnson, B. J.; Cohen, J.; Welford, R. W.; Pearson, A. R.; Schulten, K.; Klinman, J. P.; Wilmot, C. M. Exploring Molecular Oxygen Pathways in Hansenula Polymorpha Copper-Containing Amine Oxidase. *Journal of Biological Chemistry* **2007**, *282*, 17767–17776.

(28) Cohen, J.; Schulten, K. $O_2$ Migration Pathways Are Not Conserved Across Proteins of a Similar Fold. *Biophysical Journal* **2007**, *93*, 3591–3600.

(29) McDonald, W.; Funatogawa, C.; Li, Y.; Chen, Y.; Szundi, I.; Fee, J. A.; Stout, C. D.; Einarsdóttir, Ó. Conserved Glycine 232 in the Ligand Channel of Ba 3 Cytochrome Oxidase From Thermus Thermophilus. *Biochemistry* **2014**, *53*, 4467–4475.

(30) Oliveira, A. S. F.; Damas, J. M.; Baptista, A. M.; Soares, C. M. Exploring $O_2$ Diffusion in A-Type Cytochrome C Oxidases: Molecular Dynamics Simulations Uncover Two Alternative Channels Towards the Binuclear Site. *PLoS Computational Biology* **2014**, *10*, e1004010.

(31) Cohen, J.; Kim, K.; King, P.; Seibert, M.; Schulten, K. Finding Gas Diffusion Pathways in Proteins: Application to $O_2$ and $H_2$ Transport in CpI [FeFe]-Hydrogenase and the Role of Packing Defects. *Structure* **2005**, *13*, 1321–1329.

(32) Hofacker, I.; Schulten, K. Oxygen and Proton Pathways in Cytochrome C Oxidase. *Proteins Structure Function and Genetics* **1998**, *30*, 100–107.

(33) Saam, J.; Rosini, E.; Molla, G.; Schulten, K.; Pollegioni, L.; Ghisla, S. $O_2$ Reactivity of Flavoproteins Dynamic Access of Dioxygen to the Active Site and Role of a H+ Relay System in D-Amino Acid Oxidase. *Journal of Biological Chemistry* **2010**, *285*, 24439–24446.

(34) Chintapalli, S. V.; Bhardwaj, G.; Patel, R.; Shah, N.; Patterson, R. L.; van Rossum, D. B.; Anishkin, A.; Adams, S. H. Molecular Dynamic Simulations Reveal the

Structural Determinants of Fatty Acid Binding to Oxy-Myoglobin. *PLoS One* **2015**, *10*, e0128496.

(35) Wang, Y.; Cohen, J.; Boron, W. F.; Schulten, K.; Tajkhorshid, E. Exploring Gas Permeability of Cellular Membranes and Membrane Channels With Molecular Dynamics. *Journal of Structural Biology* **2007**, *157*, 534–544.

(36) Wang, P.-h.; Best, R. B.; Blumberger, J. Multiscale Simulation Reveals Multiple Pathways for $H_2$ and $O_2$ Transport in a [NiFe]-Hydrogenase. *Journal of the American Chemical Society* **2011**, *133*, 3548–3556.

(37) van Lun, M.; Hub, J. S.; van der Spoel, D.; Andersson, I. $CO_2$ and $O_2$ Distribution in Rubisco Suggests the Small Subunit Functions as a $CO_2$ Reservoir. *Journal of the American Chemical Society* **2014**, *136*, 3165–3171.

(38) Vassiliev, S.; Zaraiskaya, T.; Bruce, D. Molecular Dynamics Simulations Reveal Highly Permeable Oxygen Exit Channels Shared With Water Uptake Channels in Photosystem II. *Biochimica et Biophysica Acta (BBA) - Bioenergetics* **2013**, *1827*, 1148–1155.

(39) Gabdulkhakov, A.; Kljashtorny, V.; Dontsova, M. Analysis of Molecular Oxygen Exit Pathways in Cyanobacterial Photosystem II: Molecular Dynamics Studies. *Crystallography Reports* **2015**, *60*, 884–888.

(40) Husen, P.; Solov'yov, I. A. Mutations at the $Q_o$-Site of the Cytochrome $bc_1$ Complex Strongly Affect Oxygen Binding. *The Journal of Physical Chemistry B* **2016**, In press, DOI:10.1021/acs.jpcb.6b08226.

(41) Husen, P.; Solovyov, I. A. Spontaneous Binding of Molecular Oxygen at the $Q_o$-Site of the $bc_1$ Complex Could Stimulate Superoxide Formation. *Journal of the American Chemical Society* **2016**, *138*, 12150–12158.

(42) Salo, A. B.; Husen, P.; Solov'yov, I. A. Charge Transfer at the $Q_o$-Site of the Cytochrome $bc_1$ Complex Leads to Superoxide Production. *The Journal of Physical Chemistry B* **2016**, In Press, DOI: 10.1021/acs.jpcb.6b10403.

(43) Awoonor-Williams, E.; Rowley, C. N. Molecular Simulation of Nonfacilitated Membrane Permeation. *Biochimica et Biophysica Acta (BBA)-Biomembranes* **2016**, *1858*, 1672–1687.

(44) Mayne, C. G.; Arcario, M. J.; Mahinthichaichan, P.; Baylon, J. L.; Vermaas, J. V.; Navidpour, L.; Wen, P.-C.; Thangapandian, S.; Tajkhorshid, E. The Cellular Membrane as a Mediator for Small Molecule Interaction With Membrane Proteins. *Biochimica et Biophysica Acta (BBA) - Biomembranes* **2016**, *1858*, 2290 – 2304.

(45) Jorgensen, W. L.; Madura, J. D. Optimized Intermolecular Potential Functions for Liquid Hydrocarbons. *Journal of the American Chemical Society* **1984**, *106*, 6638–6646.

(46) Kaminski, G.; Duffy, E. M.; Matsui, T.; Jorgensen, W. L. Free Energies of Hydration and Pure Liquid Properties of Hydrocarbons From the OPLS All-Atom Model. *The Journal of Physical Chemistry* **1994**, *98*, 13077–13082.

(47) Cornell, W. D.; Cieplak, P.; Bayly, C. I.; Gould, I. R. A Second Generation Force Field for the Simulation of Proteins, Nucleic Acids, and Organic Molecules. *Journal of the American Chemical Society* **1995**, *117*, 5179–5197.

(48) MacKerell, A. D.; Bashford, D.; Bellott, M.; Dunbrack, R. L.; Evanseck, J. D.; Field, M. J.; Fischer, S.; Gao, J.; Guo, H.; Ha, S. et al. All-Atom Empirical Potential for Molecular Modeling and Dynamics Studies of Proteins. *The Journal of Physical Chemistry B* **1998**, *102*, 3586–3616.

(49) Oostenbrink, C.; Villa, A.; Mark, A. E.; van Gunsteren, W. F. A Biomolecular Force Field Based on the Free Enthalpy of Hydration and Solvation: The GROMOS Force-

Field Parameter Sets 53A5 and 53A6. *Journal of Computational Chemistry* **2004**, *25*, 1656–1676.

(50) Walter, A.; Gutknecht, J. Permeability of Small Nonelectrolytes Through Lipid Bilayer Membranes. *The Journal of Membrane Biology* **1986**, *90*, 207–217.

(51) Ben-Naim, A. Standard Thermodynamics of Transfer. Uses and Misuses. *The Journal of Physical Chemistry* **1978**, *82*, 792–803.

(52) Ben-Naim, A. *Molecular Theory of Solutions*; Oxford University Press, 2006.

(53) Ben-Naim, A. On the Evolution of the Concept of Solvation Thermodynamics. *Journal of Solution Chemistry* **2001**, *30*, 475–487.

(54) Moeser, B.; Horinek, D. The Role of the Concentration Scale in the Definition of Transfer Free Energies. *Biophysical Chemistry* **2015**, *196*, 68–76.

(55) Battino, R. The Ostwald Coefficient of Gas Solubility. *Fluid Phase Equilibria* **1984**, *15*, 231–240.

(56) Sander, R. Compilation of Henry's Law Constants for Inorganic and Organic Species of Potential Importance in Environmental Chemistry. 1999.

(57) Hesse, P. J.; Battino, R.; Scharlin, P.; Wilhelm, E. Solubility of Gases in Liquids. 20. Solubility of He, Ne, Ar, Kr, $N_2$, $O_2$, $CH_4$, $CF_4$, and $SF_6$ in n-Alkanes n-$C_lH_{2l+2}$ ($6 \leq l \leq 16$) at 298.15 K. *Journal of Chemical & Engineering Data* **1996**, *41*, 195–201.

(58) Leach, A. *Molecular Modeling - Principles and Applications*; Pearson Education Limited, 2001.

(59) Shirts, M. R.; Pitera, J. W.; Swope, W. C.; Pande, V. S. Extremely Precise Free Energy Calculations of Amino Acid Side Chain Analogs: Comparison of Common Molecular Mechanics Force Fields for Proteins. *The Journal of Chemical Physics* **2003**, *119*, 5740–22.

(60) Abraham, M. H. Free Energies, Enthalpies, and Entropies of Solution of Gaseous Nonpolar Nonelectrolytes in Water and Nonaqueous Solvents. The Hydrophobic Effect. *Journal of the American Chemical Society* **1982**, *104*, 2085–2094.

(61) Darden, T.; York, D.; Pedersen, L. Particle Mesh Ewald: An N·log (N) Method for Ewald Sums in Large Systems. *The Journal of Chemical Physics* **1993**, *98*, 10089.

(62) Essmann, U.; Perera, L.; Berkowitz, M. L.; Darden, T.; Lee, H.; Pedersen, L. G. A Smooth Particle Mesh Ewald Method. *The Journal of Chemical Physics* **1995**, *103*, 8577.

(63) Shirts, M. R.; Mobley, D. L.; Chodera, J. D.; Pande, V. S. Accurate and Efficient Corrections for Missing Dispersion Interactions in Molecular Simulations. *The Journal of Physical Chemistry B* **2007**, *111*, 13052–13063.

(64) Parrinello, M.; Rahman, A. Polymorphic Transitions in Single Crystals: A New Molecular Dynamics Method. *Journal of Applied physics* **1981**, *52*, 7182–7190.

(65) Hess, B.; Kutzner, C.; van der Spoel, D.; Lindahl, E. GROMACS 4: Algorithms for Highly Efficient, Load-Balanced, and Scalable Molecular Simulation. *Journal of Chemical Theory and Computation* **2008**, *4*, 435–447.

(66) Pronk, S.; Páll, S.; Schulz, R.; Larsson, P.; Bjelkmar, P.; Apostolov, R.; Shirts, M. R.; Smith, J. C.; Kasson, P. M.; van der Spoel, D. GROMACS 4.5: A High-Throughput and Highly Parallel Open Source Molecular Simulation Toolkit. *Bioinformatics* **2013**, *29*, 845–854.

(67) Wennberg, C. L.; Murtola, T.; Hess, B.; Lindahl, E. Lennard-Jones Lattice Summation in Bilayer Simulations Has Critical Effects on Surface Tension and Lipid Properties. *Journal of Chemical Theory and Computation* **2013**, *9*, 3527–3537.

(68) Wennberg, C. L.; Murtola, T.; Pall, S.; Abraham, M. J.; Hess, B.; Lindahl, E. Direct-Space Corrections Enable Fast and Accurate Lorentz–Berthelot Combination Rule Lennard-Jones Lattice Summation. *Journal of Chemical Theory and Computation* **2015**, *11*, 5737–5746.

(69) Páll, S.; Hess, B. A Flexible Algorithm for Calculating Pair Interactions on SIMD Architectures. *Computer Physics Communications* **2013**, *184*, 2641–2650.

(70) Boresch, S.; Archontis, G.; Karplus, M. Free Energy Simulations: The Meaning of the Individual Contributions From a Component Analysis. *Proteins: Structure, Function, and Bioinformatics* **1994**, *20*, 25–33.

(71) Beutler, T. C.; Mark, A. E.; van Schaik, R. C.; Gerber, P. R. Avoiding Singularities and Numerical Instabilities in Free Energy Calculations Based on Molecular Simulations. *Chemical Physics* **1994**, *222*, 529–539.

(72) Berendsen, H.; Postma, J.; Van Gunsteren, W.; Hermans, J. Interaction Models for Water in Relation to Protein Hydration. *Intermolecular Forces* **1981**, *11*, 331–342.

(73) Berger, O.; Edholm, O.; Jähnig, F. Molecular Dynamics Simulations of a Fluid Bilayer of Dipalmitoylphosphatidylcholine at Full Hydration, Constant Pressure, and Constant Temperature. *Biophysical Journal* **1997**, *72*, 2002–2013.

(74) Jorgensen, W. L.; Chandrasekhar, J.; Madura, J. D.; Impey, R. W.; Klein, M. L. Comparison of Simple Potential Functions for Simulating Liquid Water. *The Journal of Chemical Physics* **1983**, *79*, 926–935.

(75) Jämbeck, J. P.; Lyubartsev, A. P. Derivation and Systematic Validation of a Refined All-Atom Force Field for Phosphatidylcholine Lipids. *The Journal of Physical Chemistry B* **2012**, *116*, 3164–3179.

(76) Maciejewski, A.; Pasenkiewicz-Gierula, M.; Cramariuc, O.; Vattulainen, I.; Rog, T. Refined OPLS All-Atom Force Field for Saturated Phosphatidylcholine Bilayers at Full Hydration. *The Journal of Physical Chemistry B* **2014**, *118*, 4571–4581.

(77) Klauda, J. B.; Venable, R. M.; Freites, J. A.; O'Connor, J. W.; Tobias, D. J.; Mondragon-Ramirez, C.; Vorobyov, I.; MacKerell Jr, A. D.; Pastor, R. W. Update of the CHARMM All-Atom Additive Force Field for Lipids: Validation on Six Lipid Types. *The Journal of Physical Chemistry B* **2010**, *114*, 7830–7843.

(78) Lee, J.; Cheng, X.; Swails, J. M.; Yeom, M. S.; Eastman, P. K.; Lemkul, J. A.; Wei, S.; Buckner, J.; Jeong, J. C.; Qi, Y. et al. CHARMM-GUI Input Generator for NAMD, GROMACS, AMBER, OpenMM, and CHARMM/OpenMM Simulations Using the CHARMM36 Additive Force Field. *Journal of Chemical Theory and Computation* **2015**, *12*, 405–413.

(79) Zhang, L.; Siepmann, J. I. Direct Calculation of Henry's Law Constants From Gibbs Ensemble Monte Carlo Simulations: Nitrogen, Oxygen, Carbon Dioxide and Methane in Ethanol. *Theoretical Chemistry Accounts* **2006**, *115*, 391–397.

(80) Fischer, J. Perturbation Theory for the Free Energy of Two-Center-Lennard-Jones Liquids. *The Journal of Chemical Physics* **1980**, *72*, 5371–5377.

(81) Lide, D. *CRC Handbook of Chemistry and Physics 2009–2010 : a Ready Reference Book of Chemical and Physical Data*, 90th ed.; CRC Press: Boca Raton, 2009.

(82) Abraham, M. J.; Murtola, T.; Schulz, R.; Páll, S.; Smith, J. C.; Hess, B.; Lindahl, E. GROMACS: High Performance Molecular Simulations Through Multi-Level Parallelism From Laptops to Supercomputers. *SoftwareX* **2015**, *1*, 19–25.

(83) Wilhelm, E.; Battino, R.; Wilcock, R. J. Low-Pressure Solubility of Gases in Liquid Water. *Chemical Reviews* **1977**, *77*, 219–262.

(84) Abraham, M. H.; Andonian-Haftvan, J.; Whiting, G. S.; Leo, A.; Taft, R. S. Hydrogen Bonding. Part 34. The Factors That Influence the Solubility of Gases and Vapours in Water at 298 K, and a New Method for Its Determination. *Journal of the Chemical Society, Perkin Transactions 2* **1994**, 1777–1791.

(85) Eubank, P. Estimation of Effective Molecular Quadrupole Moments. *AIChE Journal* **1972**, *18*, 454–456.

(86) Prakash, V. Evaluation of Molecular Quadrupole Moments. *Reviews of Modern Physics* **1966**, *38*, 690.

(87) Buckingham, A. D. Permanent and Induced Molecular Moments and Long-Range Intermolecular Forces. *Advances in Chemical Physics: Intermolecular Forces, Volume 12* **1967**, 107–142.

(88) Vorobyov, I. V.; Anisimov, V. M.; MacKerell, A. D. Polarizable Empirical Force Field for Alkanes Based on the Classical Drude Oscillator Model. *The Journal of Physical Chemistry B* **2005**, *109*, 18988–18999.

(89) Anslyn, E. V.; Dougherty, D. A. *Modern Physical Organic Chemistry*; University Science Books, 2006.

(90) Mark, P.; Nilsson, L. Structure and Dynamics of the TIP3P, SPC, and SPC/E Water Models at 298 K. *The Journal of Physical Chemistry A* **2001**, *105*, 9954–9960.

(91) Han, P.; Bartels, D. M. Temperature Dependence of Oxygen Diffusion in $H_2O$ and $D_2O$. *The Journal of Physical Chemistry* **1996**, *100*, 5597–5602.

(92) Kowert, B. A.; Dang, N. C. Diffusion of Dioxygen in n-Alkanes. *The Journal of Physical Chemistry A* **1999**, *103*, 779–781.

(93) Ju, L.-K.; Ho, C. S. Oxygen Diffusion Coefficient and Solubility in n-Hexadecane. *Biotechnology and Bioengineering* **1989**, *34*, 1221–1224.

## Supporting Information Available

The following files are available free of charge. Details on the force fields and simulation parameters employed in the original publications of the earlier models.

# Supporting Information: On Atomistic Models for Molecular Oxygen

Matti Javanainen,[†,‡] Ilpo Vattulainen,[†,‡,¶] and Luca Monticelli[*,§]

†*Department of Physics, Tampere University of Technology, Tampere, Finland*

‡*Department of Physics, University of Helsinki, Helsinki, Finland*

¶*MEMPHYS - Centre for Biomembrane Physics, University of Southern Denmark, Odense, Denmark*

§*University of Lyon, CNRS, UMR 5086 MMSB, Lyon, France*

E-mail: luca.monticelli@inserm.fr

# Simulation Parameters Employed in Earlier Studies with the Benchmarked Models

Since the behavior of the $O_2$ models depends on simulation conditions, we summarize here briefly the information available on the simulation conditions that have been employed in studies with the earlier $O_2$ models.

**CHARMM**: In refs. 1,2, the CHARMM22 force field is employed together with TIP3P water model in Monte Carlo simulations. The Lorentz–Berthelot combination rules are employed. In refs. 3,4, CHARMM27 force field is used with the TIP3P water model. PME is employed for electrostatics, whereas LJ interactions are evaluated using a switch function.

**CHARMM-2**: In ref. 5, the CHARMM27 force field is employed, PME is used for electrostatics, and a cut-off of 1.2 nm is employed for LJ interactions. In ref. 6, the CHARMM27 force field is used, and electrostatics are calculated with the PME algorithm. In refs. 7, 8, and 9 the CHARMM22 force field is used. Refs. 8 and 9 state that PME is used for electrostatics, whereas the LJ cut-off is set to 1.2 nm in ref. 8. The parameters of the $O_2$ model used in refs. 7, 8, and 9 are not declared in these publications.

**CHARMM-D**: See above for parameters used in refs. 8 and 6.

**CHARMM-QR**: In the original publication (ref. 10), the Berger lipid model is employed. PME is used for electrostatics, whereas the LJ interactions are cut-off at 1 nm. In ref. 11, the OPLS all-atom force field is used together with PME for electrostatics.

**Fischer**: In ref. 12, a modified GROMOS force field is employed together with the SPC water model. LJ interactions are cut off at 0.75 nm, whereas an additional Coulomb calculation with a cut-off of 1.7 nm is performed every 10th step. In ref. 13, a united

atom model by Smondyrev and Berkowitz is used together with TIP3P water model. PME is used for electrostatics, whereas LJ interactions are cut off at 1.2 nm. The long-range dispersion correction is employed.

**Victor**: In the original publication (ref. 14), the Gromos 43A1 force field is used together with the SPC water model. The twin-range cut-off is employed with cut-offs of 0.8 and 1.4 nm. In ref. 15, the Gromos force field is employed with the SPC water model. The reaction field method is used for electrostatics with the twin range cuf-off (0.8 and 1.4 nm).

In ref. 16, the Gromos force field is employed together with the SPC water model. PME is employed for electrostatics, whereas a cut-off of 1.4 nm is employed for LJ interactions.

**Cordeiro**: In the original publication (ref. 17), the Gromos force field is used with the SPC water model. Electrostatics are calculated with PME, while a twin-range cut-off (0.9 and 1.4 nm) is used for LJ interactions. The long range dispersion correction is used.

**Porrini**: In the original publication (ref. 18), the Amber99 protein force field is employed together with the TIP3P water model. Nonbonded interactions are cut off at 1.2 nm.

**Bouanich**: In ref. 19, the Gromos force field is employed together with the SPC/E water model. PME is used for electrostatics, whereas LJ interactions are cut off at 1.4 nm. Note that $O_2$ contains a quadrupole moment in this study, yet the charges are not stated in the publication.

**Holland**: In the original publication (ref. 20), the combination of CHARMM27 (protein) and CHARMM36 (lipid) is used together with the TIP3P model for water.

**Hansen-QR**: In the original publication (ref. 21), Monte Carlo simulations are employed. The LJ cut-off is set to 1.0 nm, whereas PME is used for electrostatics. The long-range dispersion correction is applied.

**Zhang-QR**: In the original publication (ref. 22), Monte Carlo simulations are employed. The TraPPE-UA force field is used. The LJ cut-off of 1.4 nm is employed together with long-range dispersion correction. PME is used for electrostatics.

# References


(1) Jedlovszky, P.; Mezei, M. Calculation of the Free Energy Profile of $H_2O$, $O_2$, CO, $CO_2$, NO, and $CHCl_3$ in a Lipid Bilayer With a Cavity Insertion Variant of the Widom Method. *The Journal of the American Chemical Society* **2000**, *122*, 5125–5131.

(2) Jedlovszky, P.; Mezei, M. Effect of Cholesterol on the Properties of Phospholipid Membranes. 2. Free Energy Profile of Small Molecules. *The Journal of Physical Chemistry B* **2003**, *107*, 5322–5332.

(3) Shinoda, W.; Mikami, M.; Baba, T.; Hato, M. Molecular Dynamics Study on the Effects of Chain Branching on the Physical Properties of Lipid Bilayers: 2. Permeability. *The Journal of Physical Chemistry B* **2004**, *108*, 9346–9356.

(4) Shinoda, K.; Shinoda, W.; Baba, T.; Mikami, M. Comparative Molecular Dynamics Study of Ether-And Ester-Linked Phospholipid Bilayers. *The Journal of Chemical Physics* **2004**, *121*, 9648–9654.

(5) Cohen, J.; Arkhipov, A.; Braun, R.; Schulten, K. Imaging the Migration Pathways for O 2, CO, NO, and Xe Inside Myoglobin. *Biophysical Journal* **2006**, *91*, 1844–1857.

(6) Wang, Y.; Cohen, J.; Boron, W. F.; Schulten, K.; Tajkhorshid, E. Exploring Gas Per-

meability of Cellular Membranes and Membrane Channels With Molecular Dynamics. *Journal of Structural Biology* **2007**, *157*, 534–544.

(7) Cohen, J.; Kim, K.; Posewitz, M.; Ghirardi, M. L.; Schulten, K.; Seibert, M.; King, P. Molecular Dynamics and Experimental Investigation of $H_2$ and $O_2$ Diffusion in [Fe]-Hydrogenase. *Biochemical Society Transactions* **2005**, *33*, 80–82.

(8) Cohen, J.; Kim, K.; King, P.; Seibert, M.; Schulten, K. Finding Gas Diffusion Pathways in Proteins: Application to $O_2$ and $H_2$ Transport in CpI [FeFe]-Hydrogenase and the Role of Packing Defects. *Structure* **2005**, *13*, 1321–1329.

(9) Cohen, J.; Schulten, K. $O_2$ Migration Pathways Are Not Conserved Across Proteins of a Similar Fold. *Biophysical Journal* **2007**, *93*, 3591–3600.

(10) Hub, J.; de Groot, B. Mechanism of Selectivity in Aquaporins and Aquaglyceroporins. *Proceedings of the National Academy of Sciences of the United States of America* **2008**, *105*, 1198.

(11) van Lun, M.; Hub, J. S.; van der Spoel, D.; Andersson, I. $CO_2$ and $O_2$ Distribution in Rubisco Suggests the Small Subunit Functions as a $CO_2$ Reservoir. *Journal of the American Chemical Society* **2014**, *136*, 3165–3171.

(12) Marrink, S.; Berendsen, H. Permeation Process of Small Molecules Across Lipid Membranes Studied by Molecular Dynamics Simulations. *The Journal of Physical Chemistry* **1996**, *100*, 16729–16738.

(13) Sugii, T.; Takagi, S.; Matsumoto, Y. A Molecular-Dynamics Study of Lipid Bilayers: Effects of the Hydrocarbon Chain Length on Permeability. *The Journal of Chemical Physics* **2005**, *123*, 184714.

(14) Victor, B. L.; Baptista, A. M.; Soares, C. M. Dioxygen and Nitric Oxide Pathways and

Affinity to the Catalytic Site of Rubredoxin: Oxygen Oxidoreductase From Desulfovibrio Gigas. *JBIC Journal of Biological Inorganic Chemistry* **2009**, *14*, 853–862.

(15) Oliveira, A. S. F.; Damas, J. M.; Baptista, A. M.; Soares, C. M. Exploring $O_2$ Diffusion in A-Type Cytochrome C Oxidases: Molecular Dynamics Simulations Uncover Two Alternative Channels Towards the Binuclear Site. *PLoS Computational Biology* **2014**, *10*, e1004010.

(16) Damas, J. M.; Baptista, A. M.; Soares, C. M. The Pathway for O2 Diffusion Inside CotA Laccase and Possible Implications on the Multicopper Oxidases Family. *Journal of Chemical Theory and Computation* **2014**, *10*, 3525–3531.

(17) Cordeiro, R. M. Reactive Oxygen Species at Phospholipid Bilayers: Distribution, Mobility and Permeation. *Biochimica et Biophysica Acta (BBA) - Biomembranes* **2014**, *1838*, 438–444.

(18) Porrini, M.; Daskalakis, V.; Farantos, S. C. Exploring the Topography of Free Energy Surfaces and Kinetics of Cytochrome C Oxidases Interacting With Small Ligands. *RSC Advances* **2012**, *2*, 5828–5836.

(19) Wang, P.-h.; Best, R. B.; Blumberger, J. Multiscale Simulation Reveals Multiple Pathways for $H_2$ and $O_2$ Transport in a [NiFe]-Hydrogenase. *Journal of the American Chemical Society* **2011**, *133*, 3548–3556.

(20) Holland, B. W.; Berry, M. D.; Gray, C.; Tomberli, B. A Permeability Study of $O_2$ and the Trace Amine P-Tyramine Through Model Phosphatidylcholine Bilayers. *PLoS One* **2015**, *10*, e0122468.

(21) Hansen, N.; Agbor, F. A.; Keil, F. J. New Force Fields for Nitrous Oxide and Oxygen and Their Application to Phase Equilibria Simulations. *Fluid Phase Equilibria* **2007**, *259*, 180–188.

(22) Zhang, L.; Siepmann, J. I. Direct Calculation of Henry's Law Constants From Gibbs Ensemble Monte Carlo Simulations: Nitrogen, Oxygen, Carbon Dioxide and Methane in Ethanol. *Theoretical Chemistry Accounts* **2006**, *115*, 391–397.